

Inverse design of focused vector beams for mode excitation in optical nanoantennas

Xiaorun Zang,^{*} Ari T. Friberg, Tero Setälä, and Jari Turunen

Institute of Photonics, University of Eastern Finland, P.O. Box 111, FI-80101 Joensuu, Finland

(Dated: April 18, 2022)

We propose a free-space, inverse design of nanostructure's effective mode-matching fields via a backward propagation of tightly focused vector beams to the pupil plane of an aplanatic system of high numerical aperture. First, we study the nanostructure's eigenmodes without considering any excitation fields and then extract the modal near fields in the focal plane. Each modal field is then taken as the desired focal field, the band-limited waves of which are backward propagated to the pupil plane via a reversal of the Richards–Wolf vector diffraction formula. The pupil fields can be designed to be genuinely paraxial by associating the longitudinal electric/magnetic field component with the radial one on the reference sphere. The inversely designed pupil field in turn is propagated forwardly into the focal region to generate the designed focal field, whose distribution over the nanostructure's surface is used to evaluate the overlap between the designed focal field and the modal fields, i.e., the modal expansion coefficients. Studies for a silicon nanodisk monomer, dimer, and tetramer demonstrate the ability of our inverse approach to design the necessary tightly focused vector field that can effectively and exclusively match a certain eigenmode of interest. Compared with the forward beam-shaping method, the inverse design approach tends to yield quantitatively more precise mode-matching field profiles. This work can have a significant impact on optical applications that rely on controllable and tunable mode excitation and light scattering.

I. INTRODUCTION

Strong local field in plasmonic or high-index dielectric nanostructures is beneficial for boosting a variety of optical effects, via an enhanced interaction between the strong light field and nanostructures. In contrast to plasmonic systems, high-index dielectric nanoparticles, such as silicon nanodisks [1–4], do not suffer from strong optical losses but still sustain deep sub-wavelength field confinements [5]. Moreover, all-dielectric nanostructures have been demonstrated to be versatile semiconductor-compatible nanophotonic devices for directional scattering [1], near-field mapping of optical modes [6], tailoring second-harmonic [7–9] and third-harmonic [10] generations, anapole-enhanced Raman scattering [3], etc. With recent advances, all-dielectric nanostructures are promising to form basic building blocks that complement or even replace the plasmonic counterparts in modern nanophotonics [5].

At certain frequencies the local field enhancement achieves maximum values (i.e., peaks), which is a phenomenon described as the optical resonance [5, 11]. It is known that the resonance response can be tuned by varying size, shape, and dielectric environment of the nanostructures [12]. The resonance is commonly analyzed with respect to a certain incident light field, such as a plane wave used in previous studies [1, 3, 13], which, however, may not probe all resonances [14]. Recently, it has been shown that vector beams [15, 16] with spatially varying polarization distributions can reveal otherwise hidden resonances, such as the dark resonance detected by the radially or azimuthally polarized cylindrical vector beams [17–19], or the hybrid resonances by higher-order vector beams possessing helical phase distributions [20, 21].

The optical resonance response in nanostructures is associated with the excitation of one or more mode(s) [14] which, strictly speaking, are independent of any external excitation field and hence are intrinsically determined by the optical properties of the nanostructure and surrounding media. The resonance frequencies are generally isolated poles in the complex frequency plane, a characteristic of quasi-normal modes [22]. At a fixed real-valued frequency, however, a set of discrete eigenmodes [14, 23] can be defined. Modes in nanostructures have been investigated by various approaches including the electrostatic method [24–26], and several rigorous full-wave analyses based on the Fourier modal method [27–29], transfer matrix method [30], finite element method [22, 31], Green's tensor method [32], and boundary element method (BEM) based on the surface integral equations (SIEs) [14, 23, 33, 34], etc. Among them, BEM has been proven to be efficient particularly in modelling the interaction between focused vector field and nanostructures [21, 35, 36], because the numerical discretization as well as the corresponding focal fields evaluation are reduced to two dimension (2D) for a general three dimensional (3D) problem.

The excitation efficiency of an eigenmode scales with the overlap between the modal and the applied incident field profiles, as well as the corresponding eigenvalue [14]. An eigenmode's near field in optical nanoantennas is vectorial and localized such that it may vary considerably within a sub-wavelength scale, which is a fact that poses a challenge to the choice of an excitation field with an effective mode-matching profile. A free-space approach to obtain such a mode-matching vector field is to shape a focal field that is to match with the modal field, by focusing a paraxial vector beam in an aplanatic system with high numerical aperture (NA). A forward design approach has been shown to yield spatially varying field distributions for efficient hybrid mode excitations [21], but a forwardly designed focal field is limited to a qualitative mode matching due to energy exchanges between the radial and azimuthal field components in the focusing process, and then a deviation

^{*} xiaorun.zang@aalto.fi; Currently at Department of Applied Physics, Aalto University, P.O Box 13500, FI-00076 Aalto, Finland

of its field profile from the designed pupil field's. Alternatively, an inverse design is versatile in shaping focal fields that potentially bring more refined and effective mode-matching fields.

In the previous work of inverse problem in high-NA aplanatic system, the main interest has been focused on the focal field total intensity or a single component from which the complex pupil field is retrieved. For instance, the depth of focus can be optimized after determining the aberration and amplitude functions in high-NA imaging system [37], or even retrieving the birefringence from four focal field intensity distributions generated by pupil fields of different polarization states [38]. A focal field with a null longitudinal component is generated by azimuthally polarized light [39]. Needle-, tube-, and bubble-shaped focal field intensity distributions [40], perfect polarization vortex focal field [41], as well as focal field of arbitrary homogeneous polarization [42] are also investigated. However, a mode-matching focal field generally involves more than one or all field component(s) to be effectively matched with both the amplitude and phase distributions of the modal field, which has not been considered in previous work.

In this work, we present an inverse design of the desired focal field for effective mode excitation in optical nanoantennas by taking into account all modal field components and the inherent dependencies of all electric and magnetic field components in the designed beam-like pupil, reference, and focal fields. Independent of any excitation field, the eigenmodes are fully determined by the nanostructure's optical properties themselves and thus they are studied via a BEM mode solver implemented through the Müller formulation of the SIEs [43]. The modal fields in the focal plane are evaluated via the Stratton—Chu surface integral [44], and the extracted focal fields are propagated back to the pupil plane by reversing the tight focusing process. The best possible incident paraxial beams before focusing are then obtained from solving an inverse problem governed by the Richards—Wolf vector diffraction formula.

This work is organized as follows. In Sec. II, we study the eigenmodes in nanostructures, where we review the SIEs, describe the eigenvalue problem based on the Müller formulation, and analyze the eigenmodes in silicon nanodisk monomer, dimer, and tetramer. In Sec. III, we describe the forward and backward tight focusing processes which are governed by the Richards—Wolf vector diffraction formula. The degrees of freedom and strategies in our inverse design are then discussed through a systematical study of the mode-matching field design in a silicon nanodisk monomer, dimer, and tetramer. In Sec. IV, we analyze the quality of the designed focal field in terms of modal expansion coefficients, i.e., the overlaps between the designed focal field and all the first twelve eigenmodes considered in each nanodisk oligomer. At last, conclusions and perspectives are given in Sec. V.

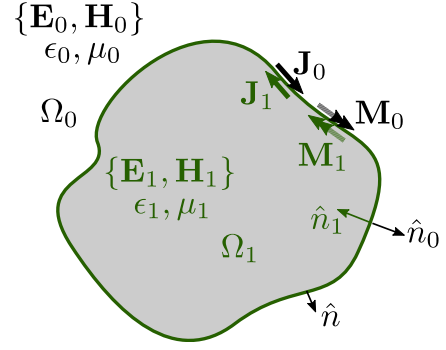


Figure 1. An arbitrarily-shaped 3D scatterer in free space. The scatterer that occupies domain Ω_1 has permittivity ϵ_1 and permeability μ_1 , whereas domain Ω_0 is free space with optical properties ϵ_0 and μ_0 . The electric and magnetic fields are $\{\mathbf{E}_0, \mathbf{H}_0\}$ in the free space and $\{\mathbf{E}_1, \mathbf{H}_1\}$ in the scatterer. Two domains' surfaces are correspondingly denoted by $\partial\Omega_0$ and $\partial\Omega_1$, and their directions are determined by normal vectors $\hat{n}_0 = \hat{n}$ and $\hat{n}_1 = -\hat{n}$. Equivalent electric and magnetic surface current densities $\{\mathbf{J}_0, \mathbf{M}_0\}$ and $\{\mathbf{J}_1, \mathbf{M}_1\}$ are mathematically introduced on $\partial\Omega_0$ and $\partial\Omega_1$, respectively.

II. EIGENMODES IN NANOSTRUCTURES

A. Surface integral equations

We first describe the eigenmode problem in optical nanostructures using the SIE formulation. Without loss of generality, the SIE formulation is reviewed for the case of a single arbitrarily shaped 3D nanostructure, since it is readily extended to more general cases of nano-object ensembles. As shown in Fig. 1, the nano-object occupying domain Ω_1 contains a homogeneous and isotropic medium with permittivity ϵ_1 and permeability μ_1 . The free space in domain Ω_0 has optical properties ϵ_0 and μ_0 . The monochromatic electric and magnetic fields of harmonic time dependence $e^{-i\omega t}$ in the scatterer and free space are denoted by $\{\mathbf{E}_1, \mathbf{H}_1\}$ and $\{\mathbf{E}_0, \mathbf{H}_0\}$, respectively, where ω is the angular frequency.

Applying the field equivalence principle [44–48] to the scatterer, we are interested in the fields $\{\mathbf{E}_1, \mathbf{H}_1\}$ in the domain Ω_1 and thus the fields elsewhere are not of interest. In this regard, the fields $\{\mathbf{E}_0, \mathbf{H}_0\}$ in the domain Ω_0 can take any values while the fields in Ω_1 are kept fixed, which in turn implies that the tangential fields over the surface $\partial\Omega_1$ of the domain Ω_1 should be unchanged, according to the uniqueness theorem [48–50]. In the equivalent problem for the scatterer, making the fields in Ω_0 trivial $\{\mathbf{E}_0 = 0, \mathbf{H}_0 = 0\}$ leads to an arbitrariness in the ϵ_0 and μ_0 values, and a convenient choice is to take the same values as in the scatterer with $\epsilon_0 = \epsilon_1$ and $\mu_0 = \mu_1$, i.e., the full space medium is homogeneous and isotropic. However, to maintain the tangential fields over $\partial\Omega_1$, equivalent electric and magnetic surface current densities must be introduced mathematically

$$\mathbf{J}_1 = \hat{n}_1 \times \mathbf{H}_1, \quad (1)$$

$$\mathbf{M}_1 = -\hat{n}_1 \times \mathbf{E}_1. \quad (2)$$

Applying the Stratton—Chu equation [44] in the equivalent problem for the scatterer, the fields of interest at a

point in the scatterer ($\mathbf{r} \in \Omega_1$) can be evaluated by

$$\begin{aligned} \mathbf{E}_1(\mathbf{r}) &= i\omega\mu_1 \iint_{\partial\Omega_1} [\mathbf{J}_1(\mathbf{r}') G_1(\mathbf{r}, \mathbf{r}')] dS' \\ &\quad - \frac{1}{i\omega\epsilon_1} \iint_{\partial\Omega_1} [\nabla' \cdot \mathbf{J}_1(\mathbf{r}') \nabla G_1(\mathbf{r}, \mathbf{r}')] dS' \\ &\quad + \iint_{\partial\Omega_1} [\mathbf{M}_1(\mathbf{r}') \times \nabla G_1(\mathbf{r}, \mathbf{r}')] dS', \end{aligned} \quad (3)$$

$$\begin{aligned} \mathbf{H}_1(\mathbf{r}) &= - \iint_{\partial\Omega_1} [\mathbf{J}_1(\mathbf{r}') \times \nabla G_1(\mathbf{r}, \mathbf{r}')] dS' \\ &\quad + i\omega\epsilon_1 \iint_{\partial\Omega_1} [\mathbf{M}_1(\mathbf{r}') G_1(\mathbf{r}, \mathbf{r}')] dS' \\ &\quad - \frac{1}{i\omega\mu_1} \iint_{\partial\Omega_1} [\nabla' \cdot \mathbf{M}_1(\mathbf{r}') \nabla G_1(\mathbf{r}, \mathbf{r}')] dS', \end{aligned} \quad (4)$$

where $G_1(\mathbf{r}, \mathbf{r}') = \exp(ik_1|\mathbf{r} - \mathbf{r}'|)/(4\pi|\mathbf{r} - \mathbf{r}'|)$ is Green's function in the whole space of the equivalent problem, and k_1 is the wave number with $k_1^2 = \epsilon_1\mu_1\omega^2$.

In the equivalent problem for the free space, the fields at a point $\mathbf{r} \in \Omega_0$ can be evaluated similarly by

$$\begin{aligned} \mathbf{E}_0(\mathbf{r}) &= \mathbf{E}_0^{(i)}(\mathbf{r}) + i\omega\mu_0 \iint_{\partial\Omega_0} [\mathbf{J}_0(\mathbf{r}') G_0(\mathbf{r}, \mathbf{r}')] dS' \\ &\quad - \frac{1}{i\omega\epsilon_0} \iint_{\partial\Omega_0} [\nabla' \cdot \mathbf{J}_0(\mathbf{r}') \nabla G_0(\mathbf{r}, \mathbf{r}')] dS' \\ &\quad + \iint_{\partial\Omega_0} [\mathbf{M}_0(\mathbf{r}') \times \nabla G_0(\mathbf{r}, \mathbf{r}')] dS', \end{aligned} \quad (5)$$

$$\begin{aligned} \mathbf{H}_0(\mathbf{r}) &= \mathbf{H}_0^{(i)}(\mathbf{r}) - \iint_{\partial\Omega_0} [\mathbf{J}_0(\mathbf{r}') \times \nabla G_0(\mathbf{r}, \mathbf{r}')] dS' \\ &\quad + i\omega\epsilon_0 \iint_{\partial\Omega_0} [\mathbf{M}_0(\mathbf{r}') G_0(\mathbf{r}, \mathbf{r}')] dS' \\ &\quad - \frac{1}{i\omega\mu_0} \iint_{\partial\Omega_0} [\nabla' \cdot \mathbf{M}_0(\mathbf{r}') \nabla G_0(\mathbf{r}, \mathbf{r}')] dS', \end{aligned} \quad (6)$$

where the extra terms $\mathbf{E}_0^{(i)}$ and $\mathbf{H}_0^{(i)}$ account for the incident fields in Ω_0 , $\mathbf{J}_0 = \hat{n}_0 \times \mathbf{H}_0$, $\mathbf{M}_0 = -\hat{n}_0 \times \mathbf{E}_0$ are the equivalent electric and magnetic surface current densities which are introduced mathematically to maintain the tangential fields on $\partial\Omega_0$, and G_0 is the full-space Green function where the corresponding wave number is k_0 with $k_0^2 = \epsilon_0\mu_0\omega^2$.

To summarize, the fields in each region are compactly written as

$$\mathbf{E}_l = \delta_{l0}\mathbf{E}_l^{(i)} + \mathcal{D}_l\mathbf{J}_l - \mathcal{K}_l\mathbf{M}_l, \quad (7)$$

$$\mathbf{H}_l = \delta_{l0}\mathbf{H}_l^{(i)} + \mathcal{K}_l\mathbf{J}_l + \left(\frac{\epsilon_l}{\mu_l}\right) \mathcal{D}_l\mathbf{M}_l. \quad (8)$$

Above, δ_{l0} is the Kronecker delta and the integro-differential operators are defined as follows,

$$\begin{aligned} \{\mathcal{D}_l\mathbf{f}(\mathbf{r}')\}(\mathbf{r}) &= i\omega\mu_l \iint_{\partial\Omega_l} [\mathbf{f}(\mathbf{r}') G_l(\mathbf{r}, \mathbf{r}')] dS' \\ &\quad - \frac{1}{i\omega\epsilon_l} \iint_{\partial\Omega_l} [\nabla' \cdot \mathbf{f}(\mathbf{r}') \nabla G_l(\mathbf{r}, \mathbf{r}')] dS', \end{aligned} \quad (9)$$

$$\{\mathcal{K}_l\mathbf{f}(\mathbf{r}')\}(\mathbf{r}) = - \iint_{\partial\Omega_l} [\mathbf{f}(\mathbf{r}') \times \nabla G_l(\mathbf{r}, \mathbf{r}')] dS', \quad (10)$$

where $l \in \{0, 1\}$ is the domain index. Therefore, for a given point on the scatterer's surface we have, after taking the operation $\hat{n}_l \times$ to Eqs. (7) and (8),

$$\mathbf{J}_l = \delta_{l0}\mathbf{J}_l^{(i)} + \hat{n}_l \times \left[\mathcal{K}_l\mathbf{J}_l + \left(\frac{\epsilon_l}{\mu_l}\right) \mathcal{D}_l\mathbf{M}_l \right], \quad (11)$$

$$\mathbf{M}_l = \delta_{l0}\mathbf{M}_l^{(i)} - \hat{n}_l \times [\mathcal{D}_l\mathbf{J}_l - \mathcal{K}_l\mathbf{M}_l], \quad (12)$$

where the current densities $\mathbf{M}_l^{(i)} = -\hat{n}_l \times \mathbf{E}_l^{(i)}$ and $\mathbf{J}_l^{(i)} = \hat{n}_l \times \mathbf{H}_l^{(i)}$ are due to the incident fields in the free space.

The N-Müller formulation [14, 43] yields stable solutions even at low-frequency limit and it can be obtained by combining the above two equations with weights μ_l and ϵ_l , as well as taking into account the tangential field continuity at the interface (i.e., $\mathbf{J} = \mathbf{J}_0 = -\mathbf{J}_1$ and $\mathbf{M} = \mathbf{M}_0 = -\mathbf{M}_1$),

$$\begin{aligned} (\mu_0 + \mu_1)\mathbf{J} &= (\mu_0\hat{n}_0 \times \mathcal{K}_0 + \mu_1\hat{n}_1 \times \mathcal{K}_1)\mathbf{J} + \mu_0\mathbf{J}_0^{(i)} \\ &\quad + (\epsilon_0\hat{n}_0 \times \mathcal{D}_0 + \epsilon_1\hat{n}_1 \times \mathcal{D}_1)\mathbf{M}, \end{aligned} \quad (13)$$

$$\begin{aligned} (\epsilon_0 + \epsilon_1)\mathbf{M} &= -(\epsilon_0\hat{n}_0 \times \mathcal{D}_0 + \epsilon_1\hat{n}_1 \times \mathcal{D}_1)\mathbf{J} + \epsilon_0\mathbf{M}_0^{(i)} \\ &\quad + (\mu_0\hat{n}_0 \times \mathcal{K}_0 + \mu_1\hat{n}_1 \times \mathcal{K}_1)\mathbf{M}. \end{aligned} \quad (14)$$

This can be further written in the compact form

$$(\mathcal{Z}_0 + \mathcal{Z}_1)\mathbf{x} = \mathbf{b}, \quad (15)$$

with the vector $\mathbf{x} = [\mathbf{J}, \mathbf{M}]$ containing the equivalent surface current densities to be solved with the knowledge of the tangential components of the incident fields $\mathbf{b} = [\mu_0\mathbf{J}_0^{(i)}, \epsilon_0\mathbf{M}_0^{(i)}]$. We also invoked the matrix notation

$$\mathcal{Z}_l = \begin{bmatrix} \mu_l & 0 \\ 0 & \epsilon_l \end{bmatrix} + \hat{n}_l \times \begin{bmatrix} -\mu_l\mathcal{K}_l & -\epsilon_l\mathcal{D}_l \\ \epsilon_l\mathcal{D}_l & -\mu_l\mathcal{K}_l \end{bmatrix}. \quad (16)$$

B. Eigenmodes

In the absence of an incident field $\mathbf{b} = 0$ holds, and the system may have nontrivial solutions at certain frequencies (usually complex-valued), each of them being associated with a resonance mode of the optical system [14, 22, 23, 33]. The resonance frequencies are generally isolated poles in the complex frequency plane. At a fixed real-valued frequency, however, we can find the scatterer's eigenmodes [14, 33] by solving

$$(\mathcal{Z}_0 + \mathcal{Z}_1)\mathbf{x}^{(m)} = \lambda^{(m)}\mathbf{x}^{(m)}. \quad (17)$$

Rewriting Eq. (17) in the form of Eq. (15), we have

$$(\mathcal{Z}_0 + \mathcal{Z}_1) \frac{\mathbf{x}^{(m)}}{\lambda^{(m)}} = \mathbf{x}^{(m)}. \quad (18)$$

Comparing Eqs. (15) and (18), it is seen that an incident field $\mathbf{x}^{(m)}$, which is the m th eigenmode, yields a scattered field $\mathbf{x}^{(m)}/\lambda^{(m)}$. In addition, an eigenmode associated with a smaller eigenvalue $\lambda^{(m)}$ yields a stronger scattered field $\mathbf{x}^{(m)}/\lambda^{(m)}$ when the scatterer is excited by an incident field of $\mathbf{x}^{(m)}$. Therefore, $1/\lambda^{(m)}$ can be viewed as the *scattering strength* associated with the m th eigenmode.

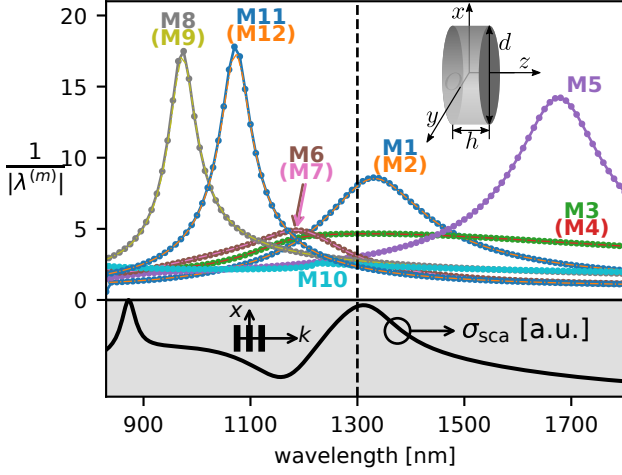


Figure 2. The reciprocal of absolute eigenvalues $1/|\lambda^{(m)}|$ of the first twelve leading eigenmodes in a silicon nanodisk in air as a function of wavelength. The nanodisk has a thickness of $h = 220$ nm and a diameter of $d = 480$ nm and it is situated at the origin of the Cartesian coordinate system (shown in the inset). Each eigenmode is labelled by M1 to M12, respectively. In case of degeneracy, one of the two degenerate eigenmodes is labelled in brackets. These twelve eigenmodes are ranked by their $1/|\lambda^{(m)}|$ values at wavelength 1300 nm (the dashed line). In the filled grey area below the zero horizontal line, the scattering cross-section (σ_{sca}) in arbitrary units is shown as the black curve when the nanodisk is illuminated by an x -polarized plane wave.

For a given eigenmode $\mathbf{x}^{(m)} = [\mathbf{J}^{(m)}, \mathbf{M}^{(m)}]$, we can calculate its electric and magnetic fields $\mathbf{E}^{(m)}$ and $\mathbf{H}^{(m)}$ everywhere, by invoking Eqs. (7) and (8),

$$\mathbf{E}_l^{(m)}(\mathbf{r}) = \mathcal{D}_l \mathbf{J}_l^{(m)} - \mathcal{K}_l \mathbf{M}_l^{(m)}, \quad (19)$$

$$\mathbf{H}_l^{(m)}(\mathbf{r}) = \mathcal{K}_l \mathbf{J}_l^{(m)} + \left(\frac{\epsilon_l}{\mu_l} \right) \mathcal{D}_l \mathbf{M}_l^{(m)}, \quad (20)$$

where the subscript l denotes the domain where the field at a given point $\mathbf{r} \in \Omega_l$ is evaluated.

C. Silicon nanodisks

Monomer

For the purpose of demonstrating the eigenmodes in all-dielectric nanostructures, we study a silicon nanodisk in air. The nanodisk has a thickness of $h = 220$ nm and a diameter of $d = 480$ nm and it is situated at the origin of the Cartesian coordinate system as shown in the inset of Fig. 2. The eigenvalues are solved in the wavelength range of [850, 1750] nm and the twelve dominant eigenmodes are shown in Fig. 2. The eigenmodes sharing the same $1/|\lambda^{(m)}|$ values are degenerate modes, whose fields are of identical distribution but distinctively oriented. Treating the degenerate eigenmodes together, we observe seven unique eigenmodes showing different resonance responses. Mode M1 (M2) has a resonance wavelength around 1330 nm. Mode M3 (M4) does not show clear resonance as its scattering strength value is flattened over a relatively wide spectral range. Mode M5 is a non-degenerate mode showing resonance scattering

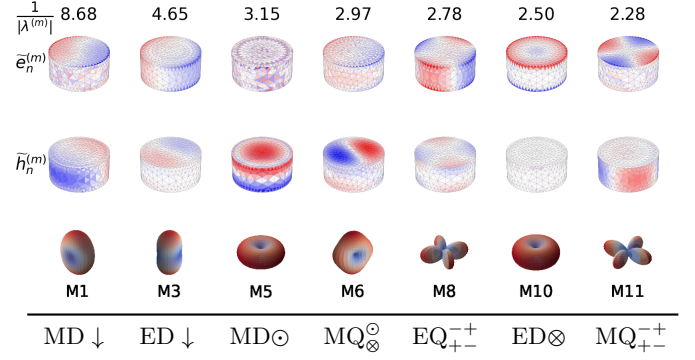


Figure 3. Near fields including the instantaneous electric $\tilde{\mathbf{e}}_n^{(m)}$ (first row) and magnetic $\tilde{\mathbf{h}}_n^{(m)}$ (second row) fields on the nanodisk's surface, and far fields (third row) of a few leading eigenmodes at the wavelength 1300 nm for the same silicon nanodisk as in Fig. 2. Each column is for one eigenmode with its $1/|\lambda^{(m)}|$ value given on the top.

at 1675 nm. Mode M6 (M7) has a relatively weak resonance near 1200 nm. Resonances at two shorter wavelengths 970 nm and 1070 nm are associated with the modes M8 (M9) and M11 (M12), respectively. At last, mode M10 is weakly resonant across the entire spectral range of interest. At this point, we emphasize that the resonance wavelengths determined from the scattering strength values are the genuine resonance wavelengths that do not depend on any external incident field. The calculated scattering cross section in arbitrary units from the nanodisk when illuminated by an x -polarized plane wave propagating along the z -axis is shown as the black curve in the filled grey area. The scattering cross section under the illumination of a linearly polarized plane wave shows a resonance peak near 1300 nm (the dashed line), at which we have ranked the aforementioned eigenmodes by their scattering strength values $1/|\lambda^{(m)}|$.

The corresponding near and far fields of the eigenmodes at the wavelength of 1300 nm are inspected in Fig. 3, and only one of degenerate eigenmodes, if any, is considered. For visualizing both the electric and magnetic near fields with balanced amplitudes [51, 52], we introduce the scaled instantaneous electric and magnetic fields as

$$\tilde{\mathbf{e}}^{(m)}(\mathbf{r}, t) = \sqrt{\epsilon_0} \text{Re} \left\{ \mathbf{E}_0^{(m)}(\mathbf{r}) e^{-i\omega t} \right\} \quad (21)$$

and

$$\tilde{\mathbf{h}}^{(m)}(\mathbf{r}, t) = \sqrt{\mu_0} \text{Re} \left\{ \mathbf{H}_0^{(m)}(\mathbf{r}) e^{-i\omega t} \right\}, \quad (22)$$

respectively, where t is a time instant, $r \in \partial\Omega_0$, and $\text{Re}\{\cdot\}$ denotes the real part. It is noted that the instantaneous electric and magnetic energy densities will be written as halves the square of the scaled instantaneous electric and magnetic fields, i.e., $w_e = [\tilde{\mathbf{e}}^{(m)}]^2/2$ and $w_h = [\tilde{\mathbf{h}}^{(m)}]^2/2$, respectively [53]. On nanodisk's surface, the normal component of the scaled field $\tilde{\mathbf{e}}_n^{(m)} = \hat{\mathbf{n}} \cdot \tilde{\mathbf{e}}^{(m)}$ at a time instant t_0 is shown for the eigenmode's electric field, and the magnetic counterpart is shown by $\tilde{\mathbf{h}}_n^{(m)} = \hat{\mathbf{n}} \cdot \tilde{\mathbf{h}}^{(m)}$ at a $\pi/2$ -phase-delayed time instant t'_0 with $\omega(t'_0 - t_0) = \pi/2$, at which time the magnetic field generally reaches its maximum.

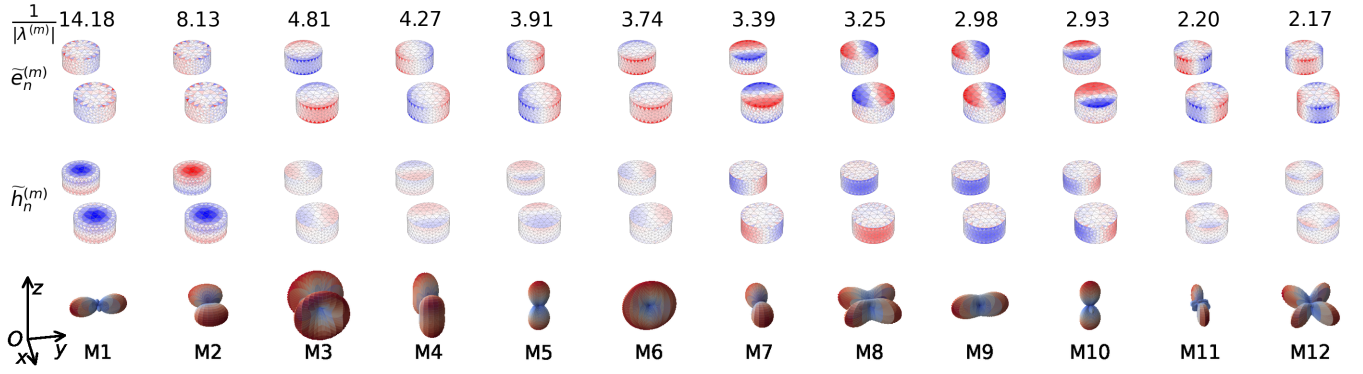


Figure 4. Near and far fields of eigenmodes M1–12 at 1600 nm in a dimer consisting of two identical silicon nanodisks (same as in Fig. 2) with a center-to-center gap of 480 nm.

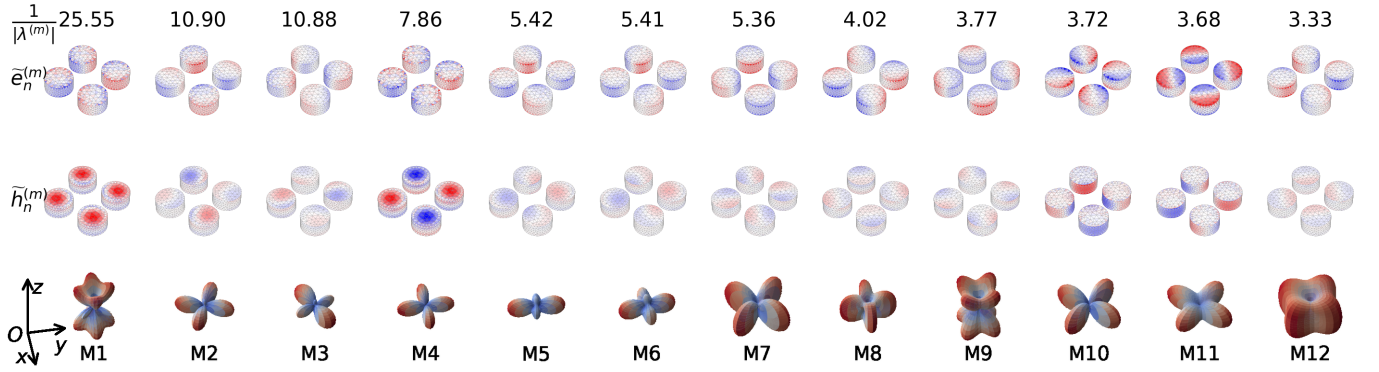


Figure 5. Near and far fields of a few leading eigenmodes M1–12 at 1600 nm in a tetramer consisting of four identical silicon nanodisks (same as in Fig. 2) with the center-to-center gap of two opposite neighbouring nanodisks being 480 nm.

For a nanodisk monomer, the surface normal near fields $\tilde{e}_n^{(m)}$ and $\tilde{h}_n^{(m)}$ are shown in the first and second rows, respectively, in Fig. 3, and the eigenmodes' corresponding far fields are shown in the third row. Each column displays the near and far fields for one eigenmode with its $1/|\lambda^{(m)}|$ value given on the top of each column. As can be seen from the radiation patterns, the eigenmode M1 is a dipolar mode showing a typical doughnut shape. Furthermore, the near fields show that the mode M1 is of magnetic dipole with a strong transverse magnetic field, which is denoted by the symbol MD \downarrow with the downarrow representing a field vector in the transverse plane. In the second column, M3 has a smaller $1/|\lambda^{(3)}|$ value, and the radiation pattern and near fields indicate that it is an electric dipolar mode, which is denoted by ED \downarrow . Under a similar observation, it turns out that M5 is a magnetic dipolar mode that differs from M1 by a dominating z magnetic field component, denoted by MD \odot with the symbol “ \odot ” implying a field vector along the positive z axis. Mode M6 emerges from a magnetic quadrupole lying in a plane parallel to the z axis, which is symbolized by MQ \otimes where the symbol “ \otimes ” implies a field vector along the negative z axis that is π -out-of-phase with respect to the “ \odot ” field vector. The mode M6 is distinct from another magnetic quadrupolar mode M11 where the quadrupole resides in the xy plane, denoted by MQ $_{+-}^{\pm}$ where the symbols “ $-$ ” and “ $+$ ” represent negative and positive field extremes, respectively. An electric quadrupolar mode, denoted by EQ $_{+-}^{\pm}$, is observed in mode M8. At last, mode M10

is an electric dipolar mode, denoted by ED \otimes , with a dominating electric z field component.

Oligomers

In silicon nanodisks ensembles, i.e., nanodisk oligomers consisting of several nanodisks, further local field enhancements and mode hybridization happen via optical near-field coupling. Here, we also investigate the near fields of a few leading eigenmodes in nanostructure assemblies that consist of two and four identical nanodisks, so-called nanodisk dimer and tetramer, respectively.

The eigenmodes' near and far fields of a dimer are shown in Fig. 4. Modes M1 and M2 are hybridized from two longitudinal magnetic dipolar modes, where the former arises from two parallel longitudinal MD modes, and the latter is due to two anti-parallel longitudinal MD modes. Transversal magnetic modes include M7–10, that are due to the hybridization of, subsequently, two y -oriented anti-parallel transversal MD modes, two x -oriented anti-parallel transversal MD modes, two x -oriented parallel transversal MD modes, and two y -oriented parallel transversal MD modes. The electric counterparts of the magnetic modes M7–10 are observed in transversal electric modes M3–6. In detail, M3 is hybridized from two x -oriented anti-parallel transversal ED modes, M4 is due to two y -oriented anti-parallel transversal ED modes, M5 arises from two y -oriented parallel transversal ED modes, and two x -oriented par-

allel transversal ED modes yields the hybrid mode M6. Additionally, two transversal EQ modes, when arranged differently, hybridize into two distinct modes M11 and M12.

In a tetramer, modes hybridization leads to more types of eigenmodes as a result of more near-field coupling channels. Near and far fields of twelve eigenmodes with leading scattering strengths $1/|\lambda^{(m)}|$ are shown in Fig. 5. It is clear that mode M1 arises from four parallel longitudinal magnetic modes, whereas the longitudinal magnetic fields in every two neighbouring nanodisks in M4 are π -out-of-phase with respect to each other. Modes hybridized from four transversal ED modes contain M7 where the ED moments are π -out-of-phase along the radial direction between every two neighbouring elements, M8 where the ED moments are π -out-of-phase between every two neighbouring elements along the azimuthal direction, M9 with radially in-phase ED moment in each element, and M12 with in-phase ED moment in each nanodisk along the azimuthal direction. Hybridization of transversal MDs leads to mode M10 with the MD moments being along the radial direction and π -out-of-phase between the neighbouring nanodisks and M11 with azimuthally in-phase MD moments. In addition, M10 and M11 are the magnetic counterparts of modes M7 and M12. It is not straightforward to gain physical insights of the origins of hybridized modes M2, M3, M5, and M6 without future investigation, and determining the near-field coupling channels for these modes is less important and not further discussed in this work.

As it can be seen from Figs. 3, 4, and 5, an eigenmode is associated with its unique near-field distribution and far-field radiation pattern. Tuning light scattered from nano-objects via selective excitation(s) of certain eigenmode(s) could serve as a basic building block for engineering optical near and/or far field(s). It is, therefore, vital to design an excitation field which highly overlaps with the field of a specific eigenmode for an effective mode excitation, i.e., mode-matching field.

III. INVERSE DESIGN VIA TIGHT FOCUSING

As shown in previous Sec. II, the eigenmode's near fields in optical nanoantennas are genuinely localized and vectorial at the nanoscale. A potential free-space approach to design such a 3D mode-matching vector field is to shape a focal field (that matches with the eigenmode's near field in optical nanoantennas that are to be placed in the vicinity of the focal point), by focusing a paraxial vector beam in an aplanatic system with high NA. In the previous work, tightly focused cylindrical vector beams of fundamental order, i.e., radially and azimuthally polarized beams [17, 18], and of higher-order polarization states [21] have been used for optical excitation of dark and hybrid modes in optical nanoantennas. In these forward design approaches, the focused field has a predefined field profile and only qualitative match of polarization distribution between the hybrid modes and the excitation fields was considered. To design the best possible focal field that quantitatively matches with the eigenmode's field, it is necessary to solve an inverse problem where the needed paraxial vec-

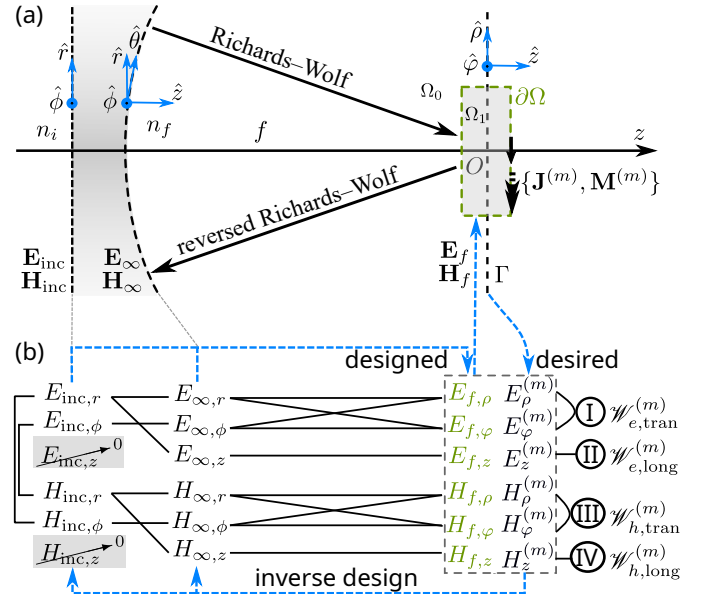


Figure 6. The inverse design scheme of focused vector beams with effective mode-matching profiles. (a) The forward and backward tight focusing processes. The nanostructure's surface is denoted by $\partial\Omega$, where the m th eigenmode's equivalent surface current density $\{\mathbf{J}^{(m)}, \mathbf{M}^{(m)}\}$ resides. The middle symmetry plane Γ coincides with the focal plane ($z = 0$ plane), where the modal field $\{\mathbf{E}^{(m)}, \mathbf{H}^{(m)}\}$ is evaluated. The reference field \mathbf{E}_∞ resides on the reference spherical cap with a radius being equal to the focal length f . The incident beam is denoted by \mathbf{E}_{inc} . The nanostructure occupies domain Ω_1 , whereas the free space is denoted by Ω_0 with a refractive index of n_f . The index before the reference sphere is denoted by n_i . (b) The inverse design flowchart. Solid black lines indicate connections between the associated field components. The modal field $\{\mathbf{E}^{(m)}, \mathbf{H}^{(m)}\}$ on the focal plane Γ serves as the desired focal field, from which the pupil field $\{\mathbf{E}_{\text{inc}}, \mathbf{H}_{\text{inc}}\}$ and thus the focal field $\{\mathbf{E}_f, \mathbf{H}_f\}$ are designed. Desired focal fields are categorized into four groups by the time-averaged energies stored in the transverse and longitudinal, electric and magnetic fields in the focal plane, denoted by $\mathscr{W}_{e,\text{tran}}^{(m)}$, $\mathscr{W}_{e,\text{long}}^{(m)}$, $\mathscr{W}_{h,\text{tran}}^{(m)}$, and $\mathscr{W}_{h,\text{long}}^{(m)}$, respectively.

tor beam to form a desired focal field after tight focusing is to be sought.

A. Tight focusing: forward and backward propagation

Before proceeding, we first review the forward and backward propagation in tight focusing of vector beams. In detail, we choose a coordinate system such that the middle plane of the nanostructure(s) coincides with the focal plane Γ (where $z = 0$), as shown in Fig. 6. For a given eigenmode, its near field $\{\mathbf{E}^{(m)}, \mathbf{H}^{(m)}\}$ is evaluated from Eqs. (19) and (20) in the focal plane Γ . For the eigenmode's electric near field to be mode-matched, a 3D vector field \mathbf{E}_f is designed via the tight focusing of a paraxial vector beam \mathbf{E}_{inc} at the pupil plane (which is mapped to \mathbf{E}_{∞} on the reference sphere).

The tight focusing process is governed by the Richards–Wolf formalism [54–56], and the focal field at a point $\mathbf{R}_f = (\rho, \varphi, z)$ in cylindrical coordinates writes

as

$$\mathbf{E}_f(\rho, \varphi, z) = \frac{-ik}{2\pi} \int_0^{\theta_{\max}} \int_0^{2\pi} \mathbf{E}_\infty(\theta, \phi) \times e^{i\mathbf{k}\cdot\mathbf{R}_f} \sin\theta d\phi d\theta, \quad (23)$$

where the wave vector \mathbf{k} is along the direction from a point on the reference sphere (ϕ, θ) to the focal point and the corresponding wave number $k = k_0$ (i.e., the same value as in domain Ω_0). The maximum converging angle $\theta_{\max} = \arcsin(\text{NA}/n_f)$ is limited by the NA of the aplanatic system, where n_f is the refractive index after the reference sphere. We can rewrite Eq. (23) into Fourier transform in Cartesian coordinates [57, 58]

$$\mathbf{E}_f(x, y, z) = \frac{-ik}{2\pi} \int_{-\infty}^{+\infty} \int_{-\infty}^{+\infty} \left[\frac{\mathbf{E}_\infty(k_x, k_y) e^{ikz \cos\theta}}{k^2 \cos\theta} \right] \times e^{-ik_x x} e^{-ik_y y} dk_x dk_y, \quad (24)$$

where $k_x = -k \sin\theta \cos\phi$ and $k_y = -k \sin\theta \sin\phi$ are the x and y components of the wave number, respectively. Here, the surface integral runs from $-\infty$ to $+\infty$, as the field \mathbf{E}_∞ on the reference sphere is zero outside of the NA. In order to obtain the necessary paraxial vector beam or the field \mathbf{E}_∞ on the reference sphere to generate the desired 3D mode-matching vector field \mathbf{E}_f , we perform the inverse Fourier transform for the above Eq. (24) except \mathbf{E}_f is replaced by the eigenmode's near field in the focal plane $\mathbf{E}^{(m)}|_\Gamma$,

$$\frac{\mathbf{E}_\infty(k_x, k_y) e^{ikz \cos\theta}}{\cos\theta} = \frac{ik}{2\pi} \int_{-\infty}^{+\infty} \int_{-\infty}^{+\infty} \mathbf{E}^{(m)}|_\Gamma \times e^{ik_x x} e^{ik_y y} dx dy, \quad (25)$$

which can be considered as the governing equation for a reversed Richards–Wolf tight focusing process.

Ideally, the paraxial input vector beam is inversely restored from the reference field [21, 59]

$$\mathbf{E}_{\text{inc}}(r, \phi) = \mathbf{L}^{-1}(\theta) \mathbf{E}_\infty(\theta, \phi), \quad (26)$$

where the radius is $r = f \sin\theta$ with f being the focal length and the mapping matrix in cylindrical coordinates is [21]

$$\mathbf{L}^{-1}(\theta) = \frac{1}{f \sqrt{\cos\theta}} \sqrt{\frac{n_f}{n_i}} \begin{bmatrix} \cos\theta & 0 & \sin\theta \\ 0 & 1 & 0 \\ -\sin\theta & 0 & \cos\theta \end{bmatrix}, \quad (27)$$

where n_i is the refractive index before the reference sphere. Above, we followed Richards and Wolf [55] for the refraction at the aplanatic lens, the reference field amplitude vector writes as $\mathbf{E}_\infty(\theta, \phi) = f \sqrt{n_i/n_f} \sqrt{\cos\theta} [E_{\text{inc},r} \hat{\theta} + E_{\text{inc},\phi} \hat{\phi} + E_{\text{inc},z}(\hat{\theta} \times \hat{\phi})]$.

B. Degrees of freedom

The associated magnetic fields are governed by similar formulas as in Eqs. (23)–(26) for the electric counterparts, but for brevity we do not repeat them here.

However, it is noted that in Richards–Wolf formalism the magnetic fields are linked to electric fields by revoking the relations $\mathbf{H}_{\text{inc}} = 1/Z_i(\mathbf{k}_i/k_i) \times \mathbf{E}_{\text{inc}}$ and thus $\mathbf{H}_\infty = 1/Z_f(\mathbf{k}_f/k_f) \times \mathbf{E}_\infty$ [54] as a result of beam-like characteristic of the vector fields on the pupil plane and on the reference sphere. Here, Z_i and Z_f are the associated wave impedances. This implies that only two components in the pupil vector field are completely independent. In cylindrical coordinates, four possible combinations of two field components are $(E_{\text{inc},r}, E_{\text{inc},\phi})$, $(H_{\text{inc},r}, H_{\text{inc},\phi})$, $(E_{\text{inc},r}, H_{\text{inc},r})$, and $(E_{\text{inc},\phi}, H_{\text{inc},\phi})$, and choosing any pair will fully determine the vector field on the pupil plane, then on the reference sphere, and finally in the focal region.

The fact that the incident vector beam is paraxial ($E_{\text{inc},z} \approx 0$ and $H_{\text{inc},z} \approx 0$) imposes a restriction on the radial and longitudinal components of the reference electric [58] and magnetic fields via the following relations:

$$-\sin\theta E_{\infty,r}(\theta, \phi) + \cos\theta E_{\infty,z}(\theta, \phi) = 0, \quad (28)$$

$$-\sin\theta H_{\infty,r}(\theta, \phi) + \cos\theta H_{\infty,z}(\theta, \phi) = 0. \quad (29)$$

As a consequence, the focused electric field \mathbf{E}_f bears all three components that are nevertheless not completely independent [39]. In other words, all three components of the electric focal field are determined uniquely by two components of the beam-like pupil field \mathbf{E}_{inc} , as seen in Fig. 6(b) where the black solid lines indicate the dependencies of field components on different planes. In order to inversely design a focal field that is truly generated by a beam-like vector pupil field, inherent dependencies of different field components of the desired focal field should be carefully investigated.

C. Inverse design strategies

To inversely design a focal field that potentially matches with an eigenmode's field, i.e., the desired focal field, in principle all the electric and magnetic modal field components should be taken into account. However, bearing in mind the degrees of freedom discussed in the previous section, an inconsistent pupil field could result from a backward propagation that ignores the inherent dependencies of all components [39] in the desired focal field. In contrast, one has to choose appropriate components in the desired focal field that will unambiguously determine the beam-like pupil field and thus the designed focal field. It is observable in Figs. 3, 4, and 5 that only some of the electric and magnetic field components are dominant in an eigenmode's near field. For instance, the mode M10 of a single nanodisk in Fig. 3 shows strong longitudinal electric field component. Moreover, in Fig. 4 modes M3–6 of a nanodisk dimer are clearly dominated by their transverse electric and longitudinal magnetic field components, whereas the transverse magnetic and longitudinal electric field components are dominant in modes M7–10 of a nanodisk dimer.

For a more quantitative analysis, we categorize the desired focal fields according to the time-averaged energies associated with the transverse and longitudinal electric and magnetic fields in the focal plane, i.e., the

following surface integrals of the energy densities [60],

$$\mathcal{W}_{e,\text{tran}}^{(m)} = \frac{1}{2} \epsilon_0 \int_{\Gamma} \left(|E_{\rho}^{(m)}|^2 + |E_{\varphi}^{(m)}|^2 \right) dS, \quad (30)$$

$$\mathcal{W}_{e,\text{long}}^{(m)} = \frac{1}{2} \epsilon_0 \int_{\Gamma} |E_z^{(m)}|^2 dS, \quad (31)$$

$$\mathcal{W}_{h,\text{tran}}^{(m)} = \frac{1}{2} \mu_0 \int_{\Gamma} \left(|H_{\rho}^{(m)}|^2 + |H_{\varphi}^{(m)}|^2 \right) dS, \quad (32)$$

$$\mathcal{W}_{h,\text{long}}^{(m)} = \frac{1}{2} \mu_0 \int_{\Gamma} |H_z^{(m)}|^2 dS. \quad (33)$$

In principle, the surface integration is performed over an infinite focal plane Γ , but in numerical evaluation we have to truncate the integration surface in an area where the desired focal field remains significant and discard the field elsewhere.

In group ①, the focal-plane energy associated with the transverse electric field is larger than those of the longitudinal electric field component as well as both focal-plane energies related to the transverse and longitudinal magnetic field components. In group ②, the focal-plane energy of the longitudinal electric field overwhelms the other three types of energies. The magnetic counterparts of groups ① and ② are group ③ and group ④, respectively. Concisely, we may write

$$\begin{aligned} & \max(\mathcal{W}_{e,\text{tran}}^{(m)}, \mathcal{W}_{e,\text{long}}^{(m)}, \mathcal{W}_{h,\text{tran}}^{(m)}, \mathcal{W}_{h,\text{long}}^{(m)}) \\ &= \begin{cases} \mathcal{W}_{e,\text{tran}}^{(m)}, & \text{in group ①,} \\ \mathcal{W}_{e,\text{long}}^{(m)}, & \text{in group ②,} \\ \mathcal{W}_{h,\text{tran}}^{(m)}, & \text{in group ③,} \\ \mathcal{W}_{h,\text{long}}^{(m)}, & \text{in group ④.} \end{cases} \end{aligned} \quad (34)$$

For eigenmodes belonging to the group ①, the corresponding transverse electric field is chosen as the candidate component of the desired focal field, upon which the radial and azimuthal components of the reference field ($E_{\infty,r}, E_{\infty,\phi}$) and thus the pupil field ($E_{\text{inc},r}, E_{\text{inc},\phi}$) are determined. The longitudinal electric focal field is, however, a free parameter so that the longitudinal electric field component on the reference sphere $E_{\infty,z}$ is determined from the radial component $E_{\infty,r}$ according to the restriction in Eq. (28). In this regard, the pupil vector field is guaranteed to be beam-like, and the designed focal field including the magnetic part is fully determined by the pair of field components ($E_{\text{inc},r}, E_{\text{inc},\phi}$).

For eigenmodes in the group ②, the longitudinal electric field component of the desired focal field $E_z^{(m)}$ determines the longitudinal electric reference field $E_{\infty,z}$, then the radial electric pupil field $E_{\text{inc},r}$ using the restriction in Eq. (28) where the radial electric reference field is a free parameter. What remains to be determined is either the azimuthal electric or the radial magnetic pupil field. But, the azimuthal electric pupil field is only determined by the azimuthal electric reference field, which in turn depends on the radial and azimuthal desired electric focal field both of which are usually trivial for an eigenmode showing strong longitudinal electric field. On the other hand, a strong longitudinal electric field component of the desired focal field is usually accompanied by slightly less stronger transverse magnetic

field component $H_{\rho}^{(m)}$ and/or $H_{\varphi}^{(m)}$ from which the radial magnetic reference field $H_{\infty,r}$ and then the radial magnetic pupil field $H_{\text{inc},r}$ can be determined. The magnetic counterparts of the aforementioned electric design strategies apply to the groups ③ and ④. At this point, it is worth pointing out that the restriction on the field components $E_{\infty,r}$ and $E_{\infty,z}$, as well as $H_{\infty,r}$ and $H_{\infty,z}$ poses a challenge to design a 3D focused vector beam, whose electric and magnetic field components perfectly match the eigenmode's near field.

Besides the constraint imposed by the beam-like characteristics in the pupil field, another limitation in the inverse design of a focal field is due to the fact that the reference field is band-limited, i.e., spatial frequencies that are larger than the free-space wave number are evanescent and cannot be backward propagated onto the reference sphere. This is associated with the fact that the tight focusing process relies on free-space beam propagation, and the focal field is actually the far field propagated from the secondary field on the reference sphere. In addition, back propagated waves are further limited by the NA of the aplanatic system.

An example eigenmode belonging to group ① is the mode M2 in the nanodisk dimer, and its scaled electric and magnetic fields at different stages of the inverse design are shown in Fig. 7. The first and second columns show all six field components of the desired focal field in the real space and spatial frequency \mathbf{k} space, respectively. The inversely designed pupil field's components are shown in the third column, and the designed focal field's components can be seen in the fourth column. Both the radial and azimuthal scaled electric field components of the designed focal field effectively match with the desired eigenmode's near field, even though the desired focal field is so locally confined that a considerable amount of light is at high spatial frequencies outside the k_0 -circle and has to be discarded in the free-space backward propagation of the inverse design. Imposed by the beam-like characteristics of the designed pupil field, the azimuthal scaled magnetic field is identical to the radial scaled electric field, whereas the radial scaled magnetic field is π -phase shifted with respect to the azimuthal scaled electric field. Four other field components are also present as a result of tight focusing of the beam-like pupil field and they are dependent on the radial and azimuthal electric field components [see Fig. 6(b) for the connections of field components]. In particular, the designed longitudinal magnetic field is π -out-of-phase with respect to the desired longitudinal magnetic field. Nevertheless, as it will be shown later with the expansion coefficients in the next section, this designed focal field still effectively excites the mode M2 in the nanodisk dimer.

Another example is shown in Fig. 8 for inversely designing a focal field to match with the eigenmode M7 in the nanodisk tetramer. An effective match between the designed and the desired focal fields is achieved in radial and azimuthal electric field components, as well as the longitudinal magnetic field component. Again, as it will be shown later with the expansion coefficients in the next section, this designed focal field can effectively and exclusively excite the mode M7 in the nanodisk tetramer. In this case, it seems dropping waves with spatial frequencies higher than those limited by

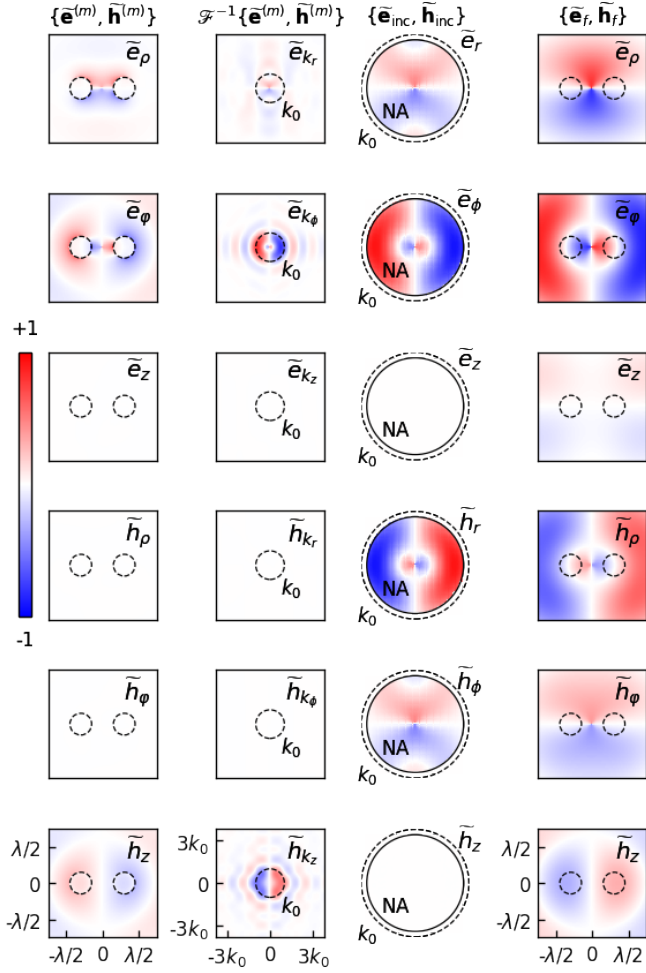


Figure 7. Scaled electric and magnetic field components [defined in Eqs. (21) and (22)] at different stages in the inverse design for M2 in the nanodisk dimer whose eigenmodes are shown in Fig. 4. The dashed circles represent the nanodisk's outlines in the desired (first column) and designed (fourth column) focal fields, or the threshold of maximum free-space wave number k_0 in \mathbf{k} space of the desired focal field (second column) and the designed pupil field (third column). The solid circle in the designed pupil field indicates the wave number limited by NA with a value of 0.9 used in this inverse design.

NA has a trivial effect on the excitation efficiency. A full list of scaled field components in the inverse design of focal field for all twelve eigenmodes in the nanodisk monomer, dimer, and tetramer is compiled in the Supplementary Material (SM).

IV. MODE EXPANSION COEFFICIENTS

Following the analysis of eigenmodes in nano-objects (Sec. II) and the inverse design of tightly focused beam (Sec. III), it is important to see how well a designed focal field matches with an eigenmode's near field. A figure of merit is the modal expansion coefficient which characterizes the overlapping between the inversely designed vector beam and the eigenmode's near field. Under the SIE formulation, the modal expansion coefficient can be evaluated via the inner product of two light fields over

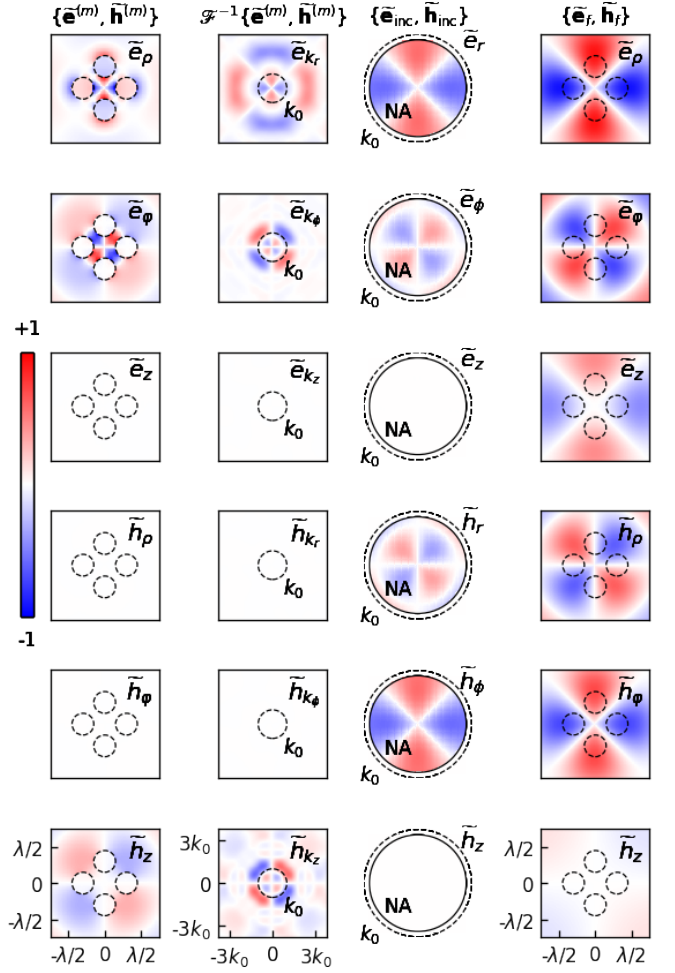


Figure 8. Scaled electric and magnetic field components in the inverse design for M7 in the nanodisk tetramer (similar to Fig. 7) whose eigenmodes are shown in Fig. 5.

the nanostructures' surfaces $\partial\Omega_0$ [14],

$$a^{(m,n)} = \frac{\iint_{\partial\Omega_0} \mathbf{x}_L^{(n)} \cdot \mathbf{b}^{(m)} dS}{\iint_{\partial\Omega_0} \mathbf{x}_L^{(n)} \cdot \mathbf{x}^{(n)} dS}, \quad (35)$$

where $\mathbf{x}_L^{(n)}$ and $\mathbf{x}^{(n)}$ are the left and right eigenvectors associated with the n th eigenmode with an eigenvalue $\lambda^{(n)}$, and $\mathbf{b}^{(m)}$ is the vector representation of the focal field inversely designed from the m th eigenmode and evaluated on the surface of the nanodisk(s) $\partial\Omega_0$. In detail, the left eigenvector is defined by, in comparison with Eq. (17),

$$\mathbf{x}_L^{(n)} (\mathcal{Z}_0 + \mathcal{Z}_1) = \lambda^{(n)} \mathbf{x}_L^{(n)}, \quad (36)$$

and the vector of the designed focal field is

$$\mathbf{b}^{(m)} = \left[\mu_0 \mathbf{J}_f^{(m)}, \epsilon_0 \mathbf{M}_f^{(m)} \right], \quad (37)$$

where $\mathbf{J}_f^{(m)} = \hat{n}_0 \times \mathbf{H}_f^{(m)}$ and $\mathbf{M}_f^{(m)} = -\hat{n}_0 \times \mathbf{E}_f^{(m)}$ are the electric and magnetic surface current densities arising from the designed focal field over the surface $\partial\Omega_0$.

The eigenmode's near field is solved directly in Eq. (17) over the surface $\partial\Omega_0$. The designed focal field on $\partial\Omega_0$ can be evaluated via the surface double integral in Eq. (23), where the reference field \mathbf{E}_∞ in the

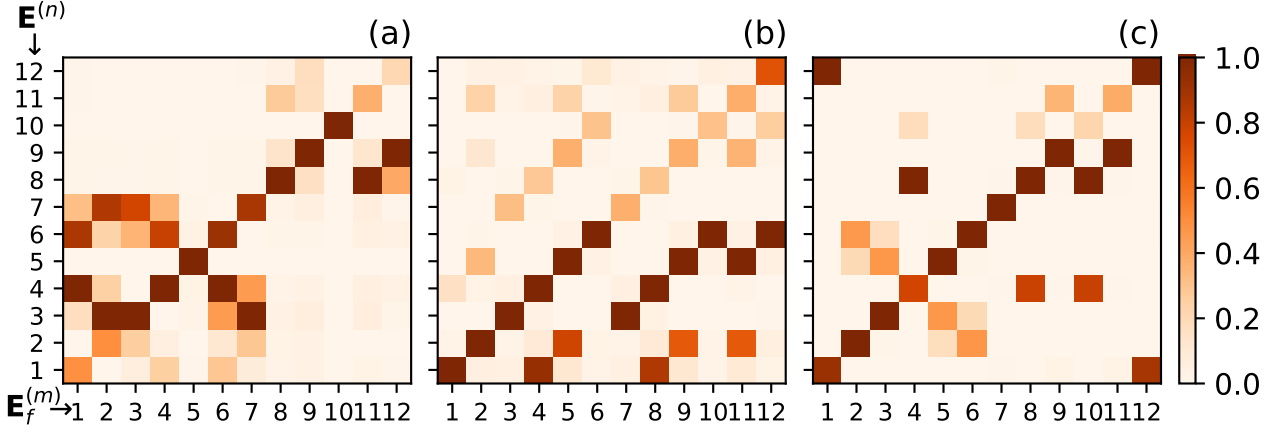


Figure 9. The mode excitation coefficients between the designed focal fields $\mathbf{E}_f^{(m)}$ (along the horizontal axis) and eigenmodes $\mathbf{E}^{(n)}$ (along the vertical axis) for the nanodisk (a) monomer, (b) dimer, and (c) tetramer. For each designed focal field, the expansion coefficients for the first twelve eigenmodes are normalized to the maximum value.

integrand is calculated through Eq. (25) by fast Fourier transform (FFT) [61]. As a result, the reference field \mathbf{E}_∞ is a 2D matrix on a square grid, and we need to use Eq. (23) rather than Eq. (24) for the focal field calculation on $\partial\Omega_0$. Here, the double integral is implemented through the 2D numerical integration based on the trapezoidal rule [62].

The expansion coefficients for the nanodisk monomer, dimer, and tetramer are visualized in three colormap matrices in Figs. 9(a), (b), and (c), respectively. The m th focal field $\mathbf{E}_f^{(m)}$ is inversely designed from the corresponding m th eigenmode's near field in the focal plane. For the monomer, the designed focal fields $\mathbf{E}_f^{(5)}$, $\mathbf{E}_f^{(8)}$, $\mathbf{E}_f^{(9)}$, and $\mathbf{E}_f^{(10)}$ largely overlap with the eigenmodes from which they are designed, respectively. In other words, these eigenmodes can be effectively mode-matched by tightly focused vector beams via our inverse design approach. However, the designed focal fields $\mathbf{E}_f^{(m)}$ with $m = 1, 2, 11$, and 12 do not effectively match the corresponding desired eigenmodes and instead other eigenmodes are strongly excited. The designed focal fields $\mathbf{E}_f^{(m)}$ with $m = 3, 4, 6$, and 7 strongly, but not exclusively (since other eigenmodes are also excited), excite the desired corresponding eigenmodes. In the nanodisk dimer case, the effective mode-matching focal fields can be obtained for the eigenmodes $\mathbf{E}^{(n)}$ with $n = 1$ to 6 , but the focal fields $\mathbf{E}_f^{(m)}$ with $m = 7$ to 12 jump to near fields that effectively match with the eigenmodes $\mathbf{E}^{(3)}$, $\mathbf{E}^{(4)}$, $\mathbf{E}^{(5)}$, $\mathbf{E}^{(6)}$, $\mathbf{E}^{(5)}$, and $\mathbf{E}^{(6)}$, respectively. For the nanodisk tetramer, the effective mode-matching focal fields are obtained for the eigenmodes $\mathbf{E}^{(n)}$ with $n = 2, 3, 5, 6, 7, 8$, and 9 . However, the designed focal fields $\mathbf{E}_f^{(10)}$ and $\mathbf{E}_f^{(11)}$ will excite the eigenmodes $\mathbf{E}^{(8)}$ and $\mathbf{E}^{(9)}$, respectively. The designed focal fields $\mathbf{E}_f^{(1)}$ and $\mathbf{E}_f^{(12)}$ always excite two eigenmodes simultaneously, including the one from which the individual focal field is inversely designed.

V. CONCLUSION AND DISCUSSION

We have developed an inverse design approach of generating a focused light field that potentially matches

with an eigenmode's near field in optical nanoantennas. We began with a rigorous analysis of eigenmodes in the optical nanoantennas of interest. In this work, a nanodisk monomer, dimer, and tetramer were considered, and the first twelve eigenmodes in each nanostructure were studied using our BEM eigenmode solver that is based on the N-Müller formulation of the SIEs. In our inverse design strategies, the eigenmode's near field in the nanodisk's middle symmetric plane (which is chosen to coincide with the focal plane) is set as the desired focal field, which is inversely propagated to the pupil plane where the designed pupil field is obtained. In this backward propagation, we took into account the beam-like characteristic of the pupil field and the fact the pupil field is band-limited, as well as the inherent dependencies of different field components. The eigenmodes were categorized into four groups by the time-averaged energies associated with the transverse and longitudinal electric and magnetic field in the focal plane, and the dominant field components were chosen for uniquely determining the beam-like pupil field. The designed focal field's expansion coefficients into the first twelve eigenmodes were evaluated. For several eigenmodes, effective and exclusive mode excitations were achieved by designing the focal field accordingly from the eigenmodes via our developed inverse design method. This work can have a significant impact on optical switching, near- and far-field engineering in nano-optics.

ACKNOWLEDGMENTS

The authors thank Martti Kauranen for valuable advice on improving the manuscript. This work was financially supported by the Academy of Finland [projects 308393 and 320166 (PREIN)].

- [1] I. Staude, A. E. Miroshnichenko, M. Decker, N. T. Fofang, S. Liu, E. Gonzales, J. Dominguez, T. S. Luk, D. N. Neshev, I. Brener, and Y. Kivshar, Tailoring directional scattering through magnetic and electric resonances in subwavelength silicon nanodisks, *ACS Nano* **7**, 7824 (2013).
- [2] K. E. Chong, I. Staude, A. James, J. Dominguez, S. Liu, S. Campione, G. S. Subramania, T. S. Luk, M. Decker, D. N. Neshev, I. Brener, and Y. S. Kivshar, Polarization-independent silicon metadevices for efficient optical wavefront control, *Nano Letters* **15**, 5369 (2015).
- [3] D. G. Baranov, R. Verre, P. Karpinski, and M. Käll, Anapole-enhanced intrinsic Raman scattering from silicon nanodisks, *ACS Photonics* **5**, 2730 (2018).
- [4] X. Zhao and B. M. Reinhard, Switchable chiroptical hot-spots in silicon nanodisk dimers, *ACS Photonics* **6**, 1981 (2019).
- [5] A. I. Kuznetsov, A. E. Miroshnichenko, M. L. Brongersma, Y. S. Kivshar, and B. Luk'yanchuk, Optically resonant dielectric nanostructures, *Science* **354**, aag2472 (2016).
- [6] T. G. Habteyes, I. Staude, K. E. Chong, J. Dominguez, M. Decker, A. Miroshnichenko, Y. Kivshar, and I. Brener, Near-field mapping of optical modes on all-dielectric silicon nanodisks, *ACS Photonics* **1**, 794 (2014).
- [7] J. Cambiasso, G. Grinblat, Y. Li, A. Rakovich, E. Cortés, and S. A. Maier, Bridging the gap between dielectric nanophotonics and the visible regime with effectively lossless GaP antennas, *Nano Letters* **17**, 1219 (2017).
- [8] R. Camacho-Morales, G. Bautista, X. Zang, L. Xu, L. Turquet, A. Miroshnichenko, H. H. Tan, A. Lamprianidis, M. Rahmani, C. Jagadish, D. N. Neshev, and M. Kauranen, Resonant harmonic generation in Al-GaAs nanoantennas probed by cylindrical vector beams, *Nanoscale* **11**, 1745 (2019).
- [9] J. D. Sautter, L. Xu, A. E. Miroshnichenko, M. Lysevych, I. Volkovskaya, D. A. Smirnova, R. Camacho-Morales, K. Zangeneh Kamali, F. Karouta, K. Vora, H. H. Tan, M. Kauranen, I. Staude, C. Jagadish, D. N. Neshev, and M. Rahmani, Tailoring second-harmonic emission from (111)-GaAs nanoantennas, *Nano Letters* **19**, 3905 (2019).
- [10] M. R. Shcherbakov, D. N. Neshev, B. Hopkins, A. S. Shorokhov, I. Staude, E. V. Melik-Gaykazyan, M. Decker, A. A. Ezhov, A. E. Miroshnichenko, I. Brener, A. A. Fedyanin, and Y. S. Kivshar, Enhanced third-harmonic generation in silicon nanoparticles driven by magnetic response, *Nano Letters* **14**, 6488 (2014).
- [11] S. A. Maier and H. A. Atwater, Plasmonics: Localization and guiding of electromagnetic energy in metal/dielectric structures, *Journal of Applied Physics* **98**, 011101 (2005).
- [12] K. L. Kelly, E. Coronado, L. L. Zhao, and G. C. Schatz, The optical properties of metal nanoparticles: The influence of size, shape, and dielectric environment, *The Journal of Physical Chemistry B* **107**, 668 (2003).
- [13] F. Moreno, P. Albella, and M. Nieto-Vesperinas, Analysis of the spectral behavior of localized plasmon resonances in the near-and far-field regimes, *Langmuir* **29**, 6715 (2013).
- [14] J. Mäkitalo, M. Kauranen, and S. Suuriniemi, Modes and resonances of plasmonic scatterers, *Physical Review B* **89**, 165429 (2014).
- [15] Q. Zhan, Cylindrical vector beams: From mathematical concepts to applications, *Advances in Optics and Photonics* **1**, 1 (2009).
- [16] C. Rosales-Guzmán, B. Ndagano, and A. Forbes, A review of complex vector light fields and their applications, *Journal of Optics* **20**, 123001 (2018).
- [17] J. Sancho-Parramon and S. Bosch, Dark modes and Fano resonances in plasmonic clusters excited by cylindrical vector beams, *ACS Nano* **6**, 8415 (2012).
- [18] D. E. Gómez, Z. Q. Teo, M. Altissimo, T. J. Davis, S. Earl, and A. Roberts, The dark side of plasmonics, *Nano Letters* **13**, 3722 (2013).
- [19] A. Yanai, M. Grajower, G. M. Lerman, M. Hentschel, H. Giessen, and U. Levy, Near-and far-field properties of plasmonic oligomers under radially and azimuthally polarized light excitation, *ACS Nano* **8**, 4969 (2014).
- [20] S. Reich, N. S. Mueller, and M. Bubula, Selection rules for structured light in nanooligomers and other nanosystems, *ACS Photonics* **7**, 1537 (2020).
- [21] X. Zang, G. Bautista, L. Turquet, T. Setälä, M. Kauranen, and J. Turunen, Efficient hybrid-mode excitation in plasmonic nanoantennas by tightly focused higher-order vector beams, *Journal of the Optical Society of America B* **38**, 521 (2021).
- [22] P. Lalanne, W. Yan, K. Vynck, C. Sauvan, and J.-P. Hugonin, Light interaction with photonic and plasmonic resonances, *Laser & Photonics Reviews* **12**, 1700113 (2018).
- [23] D. A. Powell, Resonant dynamics of arbitrarily shaped meta-atoms, *Physical Review B* **90**, 075108 (2014).
- [24] D. R. Fredkin and I. D. Mayergoyz, Resonant behavior of dielectric objects (electrostatic resonances), *Physical Review Letters* **91**, 253902 (2003).
- [25] I. D. Mayergoyz, D. R. Fredkin, and Z. Zhang, Electrostatic (plasmon) resonances in nanoparticles, *Physical Review B* **72**, 155412 (2005).
- [26] D. E. Gómez, K. C. Vernon, and T. J. Davis, Symmetry effects on the optical coupling between plasmonic nanoparticles with applications to hierarchical structures, *Physical Review B* **81**, 075414 (2010).
- [27] T. Weiss, N. A. Gippius, S. G. Tikhodeev, G. Granet, and H. Giessen, Derivation of plasmonic resonances in the Fourier modal method with adaptive spatial resolution and matched coordinates, *Journal of the Optical Society of America A* **28**, 238 (2011).
- [28] D. A. Bykov, E. A. Bezus, and L. L. Doskolovich, Use of aperiodic Fourier modal method for calculating complex-frequency eigenmodes of long-period photonic crystal slabs, *Optics Express* **25**, 27298 (2017).
- [29] D. A. Bykov and L. L. Doskolovich, Numerical methods for calculating poles of the scattering matrix with applications in grating theory, *Journal of Lightwave Technology* **31**, 793 (2013).
- [30] R. N. S. Suryadharma, M. Fruhnert, I. Fernandez-Corbaton, and C. Rockstuhl, Studying plasmonic resonance modes of hierarchical self-assembled meta-atoms based on their transfer matrix, *Physical Review B* **96**, 045406 (2017).
- [31] H. Guo, B. Oswald, and P. Arbenz, 3-dimensional eigenmodal analysis of plasmonic nanostructures, *Optics Express* **20**, 5481 (2012).
- [32] M. Paulus and O. J. F. Martin, Light propagation and scattering in stratified media: A Green's tensor approach, *Journal of the Optical Society of America A* **18**, 854 (2001).
- [33] G. D. Bernasconi, J. Butet, and O. J. Martin, Mode analysis of second-harmonic generation in plasmonic

- nanostructures, *Journal of the Optical Society of America B* **33**, 768 (2016).
- [34] D. A. Powell, Interference between the modes of an all-dielectric meta-atom, *Physical Review Applied* **7**, 034006 (2017).
 - [35] G. Bautista, M. J. Huttunen, J. Mäkitalo, J. M. Kontio, J. Simonen, and M. Kauranen, Second-harmonic generation imaging of metal nano-objects with cylindrical vector beams, *Nano Letters* **12**, 3207 (2012).
 - [36] G. Bautista, J. Mäkitalo, Y. Chen, V. Dhaka, M. Grasso, L. Karvonen, H. Jiang, M. J. Huttunen, T. Huhtio, H. Lipsanen, and M. Kauranen, Second-harmonic generation imaging of semiconductor nanowires with focused vector beams, *Nano Letters* **15**, 1564 (2015).
 - [37] R. Kant, Superresolution and increased depth of focus: An inverse problem of vector diffraction, *Journal of Modern Optics* **47**, 905 (2000).
 - [38] J. J. M. Braat, P. Dirksen, A. J. E. M. Janssen, S. van Haver, and A. S. van de Nes, Extended Nijboer–Zernike approach to aberration and birefringence retrieval in a high-numerical-aperture optical system, *Journal of the Optical Society of America A* **22**, 2635 (2005).
 - [39] M. R. Foreman, S. S. Sherif, P. R. T. Munro, and P. Török, Inversion of the Debye-Wolf diffraction integral using an eigenfunction representation of the electric fields in the focal region, *Optics Express* **16**, 4901 (2008).
 - [40] K. Jahn and N. Bokor, Solving the inverse problem of high numerical aperture focusing using vector Slepian harmonics and vector Slepian multipole fields, *Optics Communications* **288**, 13 (2013).
 - [41] Z. Chen, T. Zeng, and J. Ding, Reverse engineering approach to focus shaping, *Optics Letters* **41**, 1929 (2016).
 - [42] G. Rui, J. Chen, X. Wang, B. Gu, Y. Cui, and Q. Zhan, Synthesis of focused beam with controllable arbitrary homogeneous polarization using engineered vectorial optical fields, *Optics Express* **24**, 23667 (2016).
 - [43] P. Ylä-Oijala and M. Taskinen, Well-conditioned Muller formulation for electromagnetic scattering by dielectric objects, *IEEE Transactions on Antennas and Propagation* **53**, 3316 (2005).
 - [44] J. A. Stratton and L. J. Chu, Diffraction theory of electromagnetic waves, *Physical Review* **56**, 99 (1939).
 - [45] S. A. Schelkunoff, Some equivalence theorems of electromagnetics and their application to radiation problems, *The Bell System Technical Journal* **15**, 92 (1936).
 - [46] W. C. Chew, M. S. Tong, and B. Hu, *Integral Equation Methods for Electromagnetic and Elastic Waves* (Morgan & Claypool, 2009).
 - [47] S. J. Orfanidis, *Electromagnetic Waves and Antennas* (<https://www.ece.rutgers.edu/~orfanidi/ewa/>, 2016).
 - [48] J.-M. Jin, *Theory and Computation of Electromagnetic Fields*, 2nd ed. (John Wiley & Sons, Inc., 2015).
 - [49] R. E. Collin, *Field Theory of Guided Waves*, 2nd ed. (John Wiley & Sons, Inc., 1991).
 - [50] J. A. Kong, *Electromagnetic Wave Theory* (EMW Publishing, 2008).
 - [51] D. Colton and R. Kress, *Integral Equation Methods in Scattering Theory* (Society for Industrial and Applied Mathematics, 2013).
 - [52] M. Taskinen, *On the Implementation and Formulation of the Electromagnetic Surface Integral Equations*, Ph.D. thesis, Helsinki University of Technology (2006).
 - [53] J. D. Jackson, *Classical Electrodynamics*, 3rd ed. (Wiley, New York, 1998).
 - [54] E. Wolf, Electromagnetic diffraction in optical systems - I. An integral representation of the image field, *Proceedings of the Royal Society of London. Series A. Mathematical and Physical Sciences* **253**, 349 (1959).
 - [55] B. Richards and E. Wolf, Electromagnetic diffraction in optical systems, II. Structure of the image field in an aplanatic system, *Proceedings of the Royal Society of London. Series A. Mathematical and Physical Sciences* **253**, 358 (1959).
 - [56] S. F. Pereira and A. S. Van de Nes, Superresolution by means of polarisation, phase and amplitude pupil masks, *Optics Communications* **234**, 119 (2004).
 - [57] M. Leutenegger, R. Rao, R. Leitgeb, and T. Lasser, Fast focus field calculations, *Optics Express* **14**, 11277 (2006).
 - [58] G.-L. Zhang, X.-Z. Gao, Y. Pan, M.-D. Zhao, D. Wang, H.-H. Zhang, Y. Li, C. Tu, and H.-T. Wang, Inverse method to engineer uniform-intensity focal fields with arbitrary shape, *Optics Express* **26**, 16782 (2018).
 - [59] E. Wolf, A scalar representation of electromagnetic fields: II, *Proceedings of the Physical Society* **74**, 269 (1959).
 - [60] A. W. Snyder and J. D. Love, *Optical Waveguide Theory* (Chapman & Hall, 1983).
 - [61] M. Frigo and S. G. Johnson, The design and implementation of FFTW3, *Proceedings of the IEEE* **93**, 216 (2005).
 - [62] E. W. Cheney and D. R. Kincaid, *Numerical Mathematics and Computing*, sixth ed. (Thomson Brooks/Cole, 2007).